Journal of Materials Chemistry A

ROYAL SOCIETY OF CHEMISTRY

PAPER

View Article Online
View Journal | View Issue

Cite this: J. Mater. Chem. A, 2025, 13, 17429

Resolving the atomic structure of γ-alumina: a non-spinel phase with a distorted anion lattice and three adjacent long channels†

Xiao Yang,[a] Cheng Shang *[a] and Zhi-Pan Liu *[ab]

γ-Alumina, as a widely utilized material in human civilization for centuries, has been highly debated on its precise atomic structure. Herein we explore more than 10 million structures on the $(Al_2O_3)_xH_2O$ global potential energy surface from machine learning global optimization, and thus identify the most representative model for γ-alumina, namely the γ-AD model, which is a non-spinel phase featuring a highly distorted anion sublattice with connected voids forming three adjacent long channels. The γ-AD model is 57 meV f.u.$^{-1}$ less stable than the θ-phase and at least 40 meV f.u.$^{-1}$ more stable than all previously proposed models. Importantly, our γ-AD model reproduces correctly all minor structure patterns observed in the experiment, including the broadened small peaks below 33° in X-ray diffraction and the broadened double peak around 0.35 to 0.45 Å^{-1} in electron diffraction. The simulated surface pH_{PZC} based on γ-AD model now agrees with the experimental data, suggesting great promise for building the linkage between the γ-alumina atomic structure with its physiochemical properties from first principles.

Received 2nd March 2025
Accepted 27th April 2025

DOI: 10.1039/d5ta01715g

rsc.li/materials-a

Introduction

γ-Alumina (γ-Al_2O_3), known for its defect structure, surface acidity, high surface area, and thermal stability, is widely used as an absorbent, catalyst, and catalyst support.[1–5] However, the growth of defect-free large single γ-Al_2O_3 crystal has not been feasible despite over a century of scientific efforts. This is primarily because γ-Al_2O_3 acts as a transition phase from boehmite to α-phase[6,7] upon heating (1500 K), being less stable compared to θ- and α-phases, the growth of a defect-free large single γ-Al_2O_3 crystal has not been feasible despite over a century of scientific efforts. As a result, while many atomic structure models of γ-Al_2O_3 have been proposed in the past few decades, none of them can fully explain experimental structural data. The key questions surrounding the nature of defective sites, intrinsic disordering, and the thermodynamic stability of γ-Al_2O_3 remain open.

Fig. 1 compares the simulated X-ray diffraction (XRD) patterns and electron diffraction (ED) patterns of three representative γ-Al_2O_3 models with experimental data. All models, no matter being the spinel or non-spinel crystal structure, capture a face-centered cubic (fcc) arrangement of O anions in γ-Al_2O_3, which accounts for the XRD main peaks at $2\theta = 37.3°$, 45.9°, and 67.1° and thus can be all termed an anion-ordered γ-Al_2O_3 model. However, the broadened small peaks from 28° to 33° in

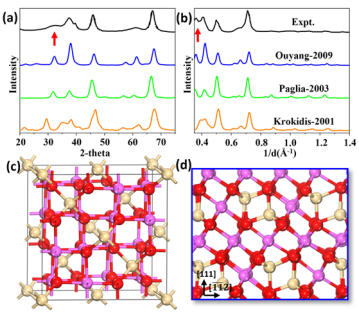

Fig. 1 Previously proposed γ-Al_2O_3 models (anion-ordered models). The simulated XRD (a) and ED (b) patterns of three representative γ-Al_2O_3 models (named by the first author and the year of publication).[8–10] The experimental data are given for comparison. (c and d) Atomic structure snapshots of (c) a perfect spinel unit cell and (d) the Ouyang-2009 model.[7,11] The lattice direction corresponding to the fcc sublattice is labeled. Purple balls: Al in octahedral sites; yellow balls: Al in tetrahedral sites; red balls: O.

[a]State Key Laboratory of Porous Materials for Separation and Conversion, Collaborative Innovation Center of Chemistry for Energy Material, Shanghai Key Laboratory of Molecular Catalysis and Innovative Materials, Key Laboratory of Computational Physical Science, Department of Chemistry, Fudan University, Shanghai 200433, China. E-mail: cshang@fudan.edu.cn; zpliu@fudan.edu.cn

[b]State Key Laboratory of Metal Organic Chemistry, Shanghai Institute of Organic Chemistry, Chinese Academy of Sciences, Shanghai 200032, China

† Electronic supplementary information (ESI) available: The computational details of the training of Al–O–H ternary G-NN potential and SSW-NN simulation; the benchmark of G-NN potential against DFT calculations; the summary of 62 metastable Al_2O_3 configurations with the fcc oxygen-lattice, their simulated XRD and ED patterns and the corresponding configurations. See DOI: https://doi.org/10.1039/d5ta01715g

XRD and the broadened double peak around 0.35 to 0.45 $Å^{-1}$ in ED[7] (see red arrows in Fig. 1), are not reproduced properly by any of the previously proposed models. These fine structural features were suggested to be caused by the intrinsic defect sites in γ-Al_2O_3,[12] *e.g.* the non-spinel site occupation. For example, Krokidis *et al.*[8] (Krokidis-2001 model in Fig. 1) performed molecular dynamics (MD) simulations of the boehmite dehydration and identified a non-spinel atomic model using a fixed orthogonal lattice (the space group $P2_1/m$), capturing the major features of the experimental XRD patterns. Paglia *et al.* (Paglia-2003 model in Fig. 1) incorporated aluminium atoms occupying non-spinel sites, which can indeed better depict the long-range pair distribution function derived from the XRD of γ-Al_2O_3 compared to conventional spinel-like models.[10] Interestingly, by superposing two different unit cells with imposed stacking faults, they further demonstrate that such a generated artificial model fits well the short-ranged pair distribution function.[13] Paglia's models, aiming to reproduce the experimental data by introducing fractionally occupied Al sites and stacking faults, not only lacks the thermodynamics basis on the stability (particularly on stacking faults), but also neglects the possible distortion of the anion sublattice (*e.g.*, deviating from the fcc lattice). Indeed, theoretical calculations show that the spinel model is more stable than the non-spinel structure. The spinel model within a relatively large unit cell (160 atoms, Ouyang-2009 model)[9,14] is 50 meV $f.u.^{-1}$ more stable than the Krokidis-2001 model and 4.2 eV $f.u.^{-1}$ more stable than Paglia's artificial model.

Herein, by machine-learning-based large-scale global potential energy surface (PES) scan, we identify an anion-distorted γ-Al_2O_3 model, named the γ-AD model, that is found to best match with experimental structural data and more importantly, is thermodynamically more stable than all previously proposed models. The defect sites of the γ-AD model originate from the fast dynamics of 66% tetrahedral Al to the nearest octahedral and tetrahedral sites as facilitated by the highly distorted O sublattice.

Results and discussion

Our global structure search was performed using the stochastic surface walking method with global neural network potential (SSW-NN method[17–23]) as implemented in LASP software (see the ESI† for all methodology details).[24,25] All likely Al–O–H compositions, including the H-containing phases, $(Al_2O_3)_x(H_2O)_y$ (x = 1–9; y = 1–2) (H may be present as OH or H_2O in the lattice) and $(Al_2O_3)_x$ have been extensively explored with various supercells containing 26–66 atoms for Al–O–H and 40/50 atoms for Al–O phases, where more than 10^7 local minima in total (4×10^5 for Al_2O_3) are visited by SSW-NN. The low-energy structures were further verified by DFT calculations, from which the global minimum (GM) for each composition was obtained (all energetic data reported in this work are from DFT). We found that the H-containing phases are generally less stable than the non-H phases based on thermodynamics (see ESI† Fig. S1 for details). This is consistent with the experimental knowledge that γ-Al_2O_3 is formed at 573–773 K, while thermogravimetry analysis (TGA) shows that H_2O desorption is completed before 773 K.[26] Hence, in the following we only focus on non-H models, which are more stable at the synthetic temperatures of γ-Al_2O_3.

Fig. 2a shows the global PES of Al–O phases (Al_2O_3) by projecting the structure fingerprint using a Steinhardt order parameter[15,16] of 125 316 distinct Al_2O_3 minima against their energy, where two large PES funnels can be distinguished at the bottom of the global PES, namely the θ-alumina funnel with the fcc O-sublattice and the α-alumina funnel with the hcp O-sublattice. We note that the θ-alumina is the GM among all Al–O phases, being 7.4 meV $f.u.^{-1}$ more stable than α-alumina. Fig. 2b further highlights the PES contour plot of 62 lowest energy minima (within 150 meV $f.u.^{-1}$ above GM) in the θ-alumina funnel, which are all non-spinel phases. Their structural data are summarized in Table S1.† By simulating the XRD and ED patterns (with Gaussian expansion, see Fig. S2 and S3† for details) of all low energy minima in Fig. 2b and comparing them with the experimental data of γ-alumina, we identify the γ-AD model that produces the best match, which locates near the bottom of the θ-alumina funnel, 57 meV $f.u.^{-1}$ above θ-alumina (ranked 9th minimum in the energy sequence) and, importantly, is 40 meV $f.u.^{-1}$ more stable than the Ouyang-2009 model. It should be emphasized that the structures (7 minima) with energy lower than the γ-AD model but higher than θ-alumina all exhibit major XRD features of θ-alumina structures (ESI Fig. S2†), suggesting they are structural distorted phases of θ-alumina. We have conducted extra SSW runs with 80–100 atoms of Al_2O_3 for more than 2×10^5 steps to verify the stability of the γ-AD model, identifying 264 extra unique minima with oxygen-sublattice packed in the fcc motif and energies within 150 meV $f.u.^{-1}$ above the GM. We find that the γ-AD model is still the most stable minima apart from the structurally distorted phases of θ-alumina.

The γ-AD model, as depicted in Fig. 2c, has a distorted fcc lattice with a unit cell of 40 atoms (a = 7.419 Å, b = 9.351 Å, c = 5.680 Å, α = 90.06°, β = 79.74, γ = 79.20°, space group $P\bar{1}$), as evidenced by 29 distinct first-neighbor O–O distances of all 144 pairs, spanning from 2.53 to 3.23 Å (*c.f.* only one possibility in a perfect fcc lattice, and 33 distinct distances of 576 pairs in the Ouyang-2009 model). The close-packed (111) surface of the oxygen sublattice (see Fig. 2c) is parallel to the (0 1 0) surface of the unit cell. 16 Al atoms fill the interstitial sites, including 6 tetrahedral Al atoms (Al_T, 37.5%) and 10 octahedral Al atoms (Al_O, 62.5%) in the unit cell. Viewed from the [001] direction of the unit cell (Fig. 2c), there are three neighbouring void-connected long channels, one 8-membered-ring void (V_8) and two 6-membered-rings (V_6), which differs from that in the θ-phase (only V_8) and Ouyang-2009 model (no large channel). The presence of these stable voids reflects the defect-creation ability and nanoporous nature of γ-alumina.

Since γ-alumina is best known for its defect structure, it is important to evaluate the dynamic behavior of ions in the lattice, which is also strongly correlated with the phase transition between different alumina phases.[27] To this end, we further performed 0.1 μs molecular dynamics (MD) simulation using G-NN under 1000 K (the upper limitation temperature for γ-Al_2O_3 synthesis), in the isothermal-isobaric (NPT) ensemble of 480-

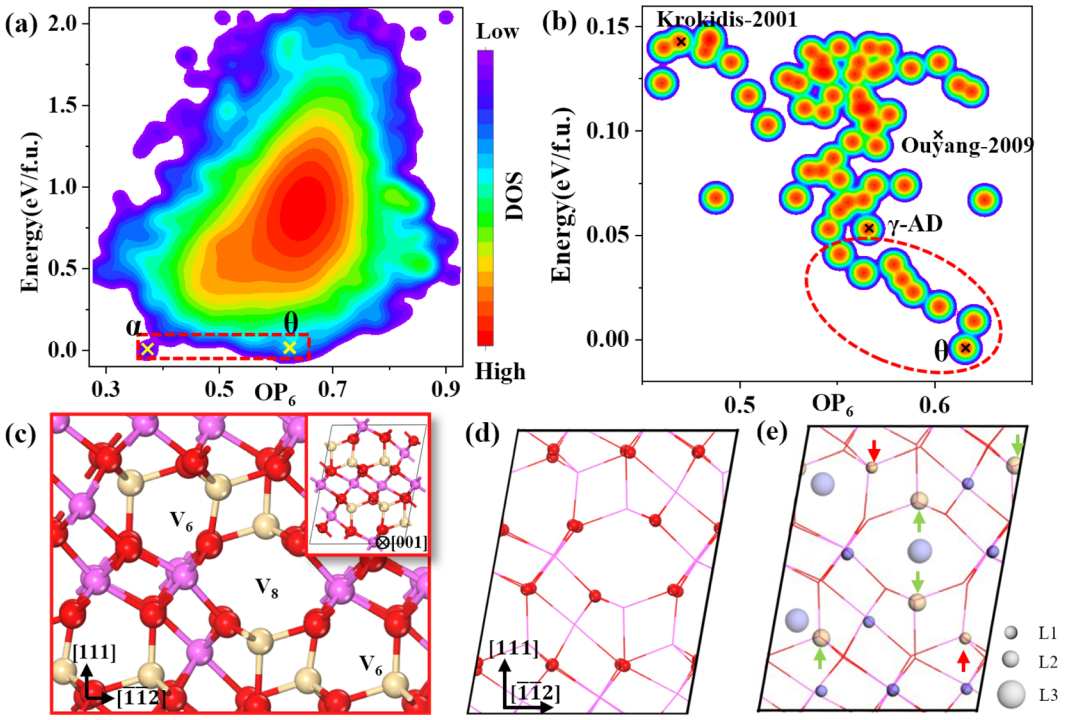

Fig. 2 Global PES of Al_2O_3 and the anion-distorted γ-Al_2O_3 model. (a) Global PES contour plot of Al_2O_3 using 125 316 distinct minima obtained from SSW-NN. The *y* axis is the energy referring to the GM (eV per formula unit, eV f.u.$^{-1}$). The *x*-axis is OP_6, the Steinhart order parameter with "l" in the spherical harmonic function equal to 6.[15,16] The dashed red box indicates the boundary of (b). (b) The PES contour plot of the bottom of the fcc O sublattice funnel, 62 structures within 0.15 eV f.u.$^{-1}$ above the GM. The θ phase, our model (γ-AD), Ouyang-2009 model and Krokidis-2001 model are labeled using black cross marks. (c) The atomic structure of the γ-AD model. The lattice direction corresponding to the fcc sublattice is labeled. The 8-membered-ring void (V_8) and 6-membered-ring void (V_6) channels are highlighted. The unit cell at the same view angle is shown in the inset. The color scheme for the atoms is the same as in Fig. 1. (d and e) The dynamic behavior of the O anion (c) and Al cation (d) from a 0.1 μs MD trajectory of the γ-AD model at 1000 K. The size of the ball (red: fcc sublattice site, yellow: tetrahedral site; magenta: octahedral site) from small to large reflects the overall occupancy probability P_{occ} of each site (relative to the γ-AD model) from high to low (L1 to L3).

atom simulation cell for the γ-AD model and compared it with that of θ-alumina. We selected one structure every 10 ns from the MD trajectory and benchmarked the G-NN potential with DFT calculations, showing an average energy error of 3.01 meV per atom. After the first 10 ps for equilibrium, the snapshots were taken from the MD trajectories every 0.1 ps from all MD trajectories and optimized to the local minima (the inherent structure). We found that there is no appreciable atomic diffusion in θ-alumina within the long simulation time (0.1 μs). In contrast, from the γ-AD model trajectory, we obtained 831 distinct local minima, suggesting a highly dynamic nature of the γ-AD structure. By calculating the overall occupancy probability of each site statistically, *i.e.*, P_{occ}, the overall occupied duration time divided by the total simulation time (0.1 μs), we can resolve the physical origin of the structure dynamics. The results for the O anion and Al cation are shown in Fig. 2d and e, respectively, where the size of the ball reflects the stability of the site—the larger the ball is, the less time the site is occupied.

We found that (i) all O anions (red balls in Fig. 2d) only vibrate at the equilibrium lattice sites, despite the sublattice deviating largely from the perfect fcc lattice and the cation motion and (ii) it is Al cations that migrate between the interstitial sites. The extent of the migration can be classified into three levels as visualized from the ball size in Fig. 2e. The most immobile site (L1 in Fig. 2e) corresponds to $P_{occ} > 99\%$, which includes all the occupied octahedral sites and two occupied tetrahedral sites (red arrows in Fig. 2e); the second level (L2) corresponds to $P_{occ} > 90\%$, including the rest four occupied tetrahedral sites (green arrows); and the third level (L3) corresponds to $P_{occ} = 7$–4%, including four void octahedral sites next to the tetrahedral sites at the L2 level, suggesting their fast interexchange. Overall, 20 different octahedral and tetrahedral sites per unit cell (16 Al atoms) can be occupied; in particular, the total occupancy of the tetrahedral site is 5.78 in the 40-atom unit cell, reduced by 22% compared to the static γ-AD model, corresponding to 36% of all the Al atoms. This agrees nicely with the important experimental fact on γ-alumina that the Al_T takes 32–37% from Al^{27} NMR.[28] The chemical shift between Al_T and Al_O in the γ-AD model is 57.7 ± 3.8 ppm, being consistent with the literature.[29–31] To further check the MD results in 0.1 μs at 1000 K, we also speeded up the MD simulation by elevating temperature to 1800 K (Fig. S4†). The results are basically the same, which confirms the rigidity of the O sublattice but exhibits more rapid cation dynamics.

Importantly, we find that by considering the cation dynamics at finite temperatures, the XRD pattern of the γ-AD model can even better match with the experimental data. Using a 2 × 2 × 1 supercell of γ-AD and considering all possible Al migration

according to MD simulations, we obtained 156 most stable bulk structures and their corresponding nanoparticle models, which were built following the proposed rhombic motif.[32] The lengths of the three edges of the models are 11.6, 5.5, and 2.5 nm, respectively (Fig. S5†). The final XRD and ED patterns (Fig. 3a) are an average over these particles, weighted by the Boltzmann distribution of the potential energy of their bulk. These patterns of γ-AD match excellently with the experimental data, as both the positions and the intensity rank of the main peaks correspond well with the experimental results.

Table 1 lists the key structural features of the γ-AD model, including the Miller indices of the diffraction peaks, their correspondence to the Miller indices of the fcc sublattice, and the origin of the diffraction peaks, as further elaborated below. The details of XRD peaks within the 28–33° range are summarized in Table S4.† The main structural features of γ-AD include three major peaks, 37.3°, 45.9°, and 67.1°, in XRD (Fig. 3a), also 0.43 $Å^{-1}$, 0.52 $Å^{-1}$, and 0.72 $Å^{-1}$ in ED (Fig. 3b). Importantly, the minor broadening peaks below 33° in XRD and 0.35–0.45 $Å^{-1}$ broadened double small peaks in ED are now captured correctly by the γ-AD model. The radial pair distribution function (RDF, $g(r)$) between atoms can provide more detailed knowledge on the atom distribution. As shown in Fig. 3c, the Al_T atoms ($g(Al_T–Al_T)$) have two types of local connectivity, a smaller peak at 2.82 Å for Al_T sharing one O atom and a larger peak at 3.45 Å involving two Al_T atoms separated by an unoccupied octahedral site. By contrast, the Al_O atoms exhibit a strong preference for sharing edges with nearby Al_O atoms, manifested by the large peak at 2.82 Å in the RDF of $g(Al_O–Al_O)$. The local connectivity between Al_T and Al_O atoms is through the sharing of corner oxygen atoms, as reflected by the dominant peak at 3.3 Å in the RDF of $g(Al_o–Al_T)$. We note that the Ouyang-2009 model lacks the first (2.82 Å), the third (4.47 Å) and the fourth (4.89 Å) peaks between two Al_T (red curve in $g(Al_T–Al_T)$), thus appears to be more crystalline compared to our γ-AD model. Moreover, from the g(O–O) patterns (Fig. 3c), we observe a large oxygen lattice distortion. For instance, the signal at 2.82 Å corresponds to the [110] orientation and 3.98 Å corresponds to the [100] orientation of the perfect fcc oxygen sublattice both split into two peaks.

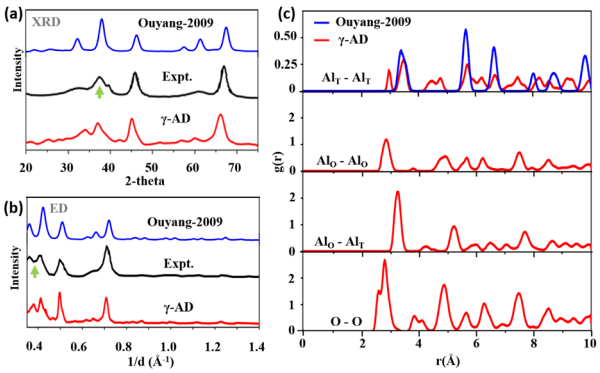

Fig. 3 (a and b) The simulated XRD (a) and ED (b) of γ-AD particle models in comparison with experimental results and the Ouyang-2009 model. (c) The RDF of the γ-AD model (red) from different atomic pairs. The blue curve in $Al_T–Al_T$ corresponds to the result from the Ouyang-2009 model.

Table 1 Structural correspondence of the γ-AD model. Listed data include the Miller index of major diffraction peaks in XRD, ED patterns in the γ-AD lattice and in the ideal fcc sublattice "$(hkl)_{fcc}$", and their RDF information

			RDF		
(hkl) γ-AD	XRD (°)	ED ($Å^{-1}$)	r (Å)	Pair	$(hkl)_{fcc}$
(104)	67.1	0.72	2.82	$Al_T–Al_T$	(440)
($\bar{4}12$)				$Al_O–Al_O$	
($\bar{1}52$)				O–O	
($\bar{1}5\bar{2}$)	60.5	0.65	5.17	Al_T–O	(115)
(252)				$Al_O–Al_T$	
($\bar{1}3\bar{2}$)	45.6	0.50	1.99	Al_O–O	(400)
(232)					
($3\bar{2}0$)					
($2\bar{1}2$)	39.5	0.43	1.72	Al_T–O	(222)
($\bar{1}12$)			5.17	$Al_O–Al_T$	
(212)	37.3	0.42	3.30	$Al_O–Al_T$	(311)
($\bar{1}\bar{1}2$)				Al_T–O	
(300)					
($\bar{2}11$)	34.5	0.39	4.88	$Al_T–Al_T$	(7,1$\bar{3}$,9)
(1$\bar{3}$0)				$Al_O–Al_O$	(7,15,$\bar{7}$)
				O–O	
(131)	32.5	0.36	3.30	$Al_O–Al_T$	(3,$\bar{3}$,11)
(0$\bar{3}$1)				Al_T–O	(31,15,$\bar{7}$)

Finally, it is interesting to link the γ-AD structure with its physicochemical properties. We examined the surface point-of-zero charge, *i.e.*, the pH_{PZC}, using our γ-AD model, which is a basic surface property of oxides. Our simulation was carried out in a (110) slab that exposes in an aqueous solution. The γ-Al_2O_3/water interface at the thermal equilibrium was first achieved using SSW exploration followed by MD simulation.[33] In total 1.375 monolayer water is found to adsorb on the surface, 59% dissociative and 41% molecularly (Fig. S6†). These dissociated H and OH will contribute to surface acidity. By further carrying out free energy calculations with umbrella sampling,[34,35] we obtained the surface deprotonation (ΔG_d) and protonation (ΔG_p) free energy change, being $\Delta G_d = 0.34 \pm 0.01$ eV and $\Delta G_p = 0.17 \pm 0.01$ eV (Fig. S7†). This leads to the computed pH_{PZC}[36] as 8.34 ± 0.17 (see the ESI†), which falls nicely within the range of experimental values of 8–8.6.[37] It might be mentioned that the previous theoretical results are obviously too low (6.67) using the spinel model.[38]

Conclusion

To recap, machine learning-based global PES exploration reveals the most representative structure model of γ-alumina, the γ-AD model. It has a highly distorted anion sublattice with neighbouring 8-membered-ring and 6-membered-ring void channels, which generates a rich cation dynamics flexibility. This γ-AD model explains the long-standing puzzles on the structural features obtained from XRD and ED in the experiment and should open a new era for understanding and designing γ-alumina based materials.

Data availability

All data are available within the article and its ESI† files. The software of LASP is available on the website **http://**

www.lasphub.com. The NN potential and the corresponding training dataset can be downloaded from the following: http://www.lasphub.com/supportings/AlOH.pot & http://www.lasphub.com/supportings/Trainfile_AlOH.tar.gz.

Author contributions

C. Shang & Z.-P Liu conceived the project and contributed to the design of the calculations and analyses of the data. X. Yang carried out most of the calculations and wrote the draft of the paper. All the authors discussed the results and commented on the manuscript.

Conflicts of interest

There are no conflicts to declare.

Acknowledgements

This work was supported by the National Science Foundation of China (12188101, 22033003, 22122301, and 92472113), the National Key Research and Development Program of China (2024YFA1509600), the Fundamental Research Funds for the Central Universities (20720220011), Science & Technology Commission of Shanghai Municipality (2024ZDSYS02), and the Tencent Foundation for XPLORER PRIZE.

Notes and references

1 H. Knozinger and P. Ratnasamy, *Catal. Rev.:Sci. Eng.*, 1978, **17**, 31–70.
2 Z. Xu, F. S. Xiao, S. K. Purnell, O. Alexeev, S. Kawi, S. E. Deutsch and B. C. Gates, *Nature*, 1994, **372**, 346–348.
3 E. J. Peterson, A. T. DeLaRiva, S. Lin, R. S. Johnson, H. Guo, J. T. Miller, J. Hun Kwak, C. H. F. Peden, B. Kiefer, L. F. Allard, F. H. Ribeiro and A. K. Datye, *Nat. Commun.*, 2014, **5**, 4885.
4 F. Zhang, M. Zeng, R. D. Yappert, J. Sun, Y.-H. Lee, A. M. LaPointe, B. Peters, M. M. Abu-Omar and S. L. Scott, *Science*, 2020, **370**, 437–441.
5 G. D. Sun, Z. J. Zhao, R. T. Mu, S. J. Zha, L. L. Li, S. Chen, K. T. Zang, J. Luo, Z. L. Li, S. C. Purdy, A. J. Kropf, J. T. Miller, L. Zeng and J. L. Gong, *Nat. Commun.*, 2018, **9**, 4454.
6 I. Levin and D. Brandon, *J. Am. Ceram. Soc.*, 1998, **81**, 1995–2012.
7 H. O. Ayoola, S. D. House, C. S. Bonifacio, K. Kisslinger, W. A. Saidi and J. C. Yang, *Acta Mater.*, 2020, **182**, 257–266.
8 X. Krokidis, P. Raybaud, A.-E. Gobichon, B. Rebours, P. Euzen and H. Toulhoat, *J. Phys. Chem. B*, 2001, **105**, 5121–5130.
9 C. Y. Ouyang, Z. Sljivancanin and A. Baldereschi, *Phys. Rev. B:Condens. Matter Mater. Phys.*, 2009, **79**, 235410.
10 G. Paglia, C. E. Buckley, A. L. Rohl, B. A. Hunter, R. D. Hart, J. V. Hanna and L. T. Byrne, *Phys. Rev. B:Condens. Matter Mater. Phys.*, 2003, **68**, 144110.
11 R. S. Zhou and R. L. Snyder, *Acta Crystallogr., Sect. B: Struct. Sci.*, 1991, **47**, 617–630.
12 V. P. Pakharukova, D. A. Yatsenko, E. Y. Gerasimov, A. S. Shalygin, O. N. Martyanov and S. V. Tsybulya, *J. Solid State Chem.*, 2017, **246**, 284–292.
13 G. Paglia, E. S. Bozin and S. J. L. Billinge, *Chem. Mater.*, 2006, **18**, 3242–3248.
14 H. Zhou, Y. Ji, Y. Wang, K. Feng, B. Luan, X. Zhang and L.-Q. Chen, *Acta Mater.*, 2024, **263**, 119513.
15 P. J. Steinhardt, D. R. Nelson and M. Ronchetti, *Phys. Rev. B:Condens. Matter Mater. Phys.*, 1983, **28**, 784–805.
16 X.-J. Zhang, C. Shang and Z.-P. Liu, *Phys. Chem. Chem. Phys.*, 2017, **19**, 4725–4733.
17 C. Shang, X.-J. Zhang and Z.-P. Liu, *Phys. Chem. Chem. Phys.*, 2014, **16**, 17845–17856.
18 C. Shang and Z.-P. Liu, *J. Chem. Theory Comput.*, 2013, **9**, 1838–1845.
19 S.-D. Huang, C. Shang, X.-J. Zhang and Z.-P. Liu, *Chem. Sci.*, 2017, **8**, 6327–6337.
20 P.-L. Kang, Z.-X. Yang, C. Shang and Z.-P. Liu, *J. Chem. Theory Comput.*, 2023, **19**, 7972–7981.
21 D. Chen, L. Chen, Q.-C. Zhao, Z.-X. Yang, C. Shang and Z.-P. Liu, *Nat. Catal.*, 2024, **7**, 536–545.
22 Q.-Y. Liu, C. Shang and Z.-P. Liu, *J. Am. Chem. Soc.*, 2021, **143**, 11109–11120.
23 Y. F. Li and Z. P. Liu, *Phys. Rev. Lett.*, 2022, **128**, 226102.
24 S.-D. Huang, C. Shang, P.-L. Kang, X.-J. Zhang and Z.-P. Liu, *Wiley Interdiscip. Rev.: Comput. Mol. Sci.*, 2019, **9**, e1415.
25 P.-L. Kang, C. Shang and Z. Liu, *Chin. J. Chem. Phys.*, 2021, **34**, 583.
26 N. Lock, P. Hald, M. Christensen, H. Birkedal and B. B. Iversen, *J. Appl. Crystallogr.*, 2010, **43**, 858–866.
27 X. Yang, C. Shang and Z.-P. Liu, *Chin. J. Chem. Phys.*, 2024, **37**, 465–470.
28 L. Kovarik, M. Bowden, A. Andersen, N. R. Jaegers, N. Washton and J. Szanyi, *Angew. Chem., Int. Ed. Engl.*, 2020, **59**, 21719–21727.
29 K. Khivantsev, N. R. Jaegers, J.-H. Kwak, J. Szanyi and L. Kovarik, *Angew. Chem., Int. Ed.*, 2021, **60**, 17522–17530.
30 R. Wischert, P. Florian, C. Copéret, D. Massiot and P. Sautet, *J. Phys. Chem. C*, 2014, **118**, 15292–15299.
31 J. Lee, H. Jeon, D. G. Oh, J. Szanyi and J. H. Kwak, *Appl. Catal., A*, 2015, **500**, 58–68.
32 Y. Sakashita, Y. Araki and H. Shimada, *Appl. Catal., A*, 2001, **215**, 101–110.
33 L.-H. Luo, S.-D. Huang, C. Shang and Z.-P. Liu, *ACS Catal.*, 2022, **12**, 6265–6275.
34 G. M. Torrie and J. P. Valleau, *J. Comput. Phys.*, 1977, **23**, 187–199.
35 Z.-Y. Hu, L.-H. Luo, C. Shang and Z.-P. Liu, *ACS Catal.*, 2024, **14**, 7684–7695.
36 B. Wen, M. F. Calegari Andrade, L.-M. Liu and A. Selloni, *Proc. Natl. Acad. Sci. U.S.A.*, 2023, **120**, e2212250120.
37 K. Bourikas, J. Vakros, C. Kordulis and A. Lycourghiotis, *J. Phys. Chem. B*, 2003, **107**, 9441–9451.
38 G. Di Liberto, F. Maleki and G. Pacchioni, *J. Phys. Chem. C*, 2022, **126**, 10216–10223.